On the Generation of Gapless and Seamless Daily Surface Reflectance Data

Gang Yang, Huanfeng Shen, *Senior Member, IEEE*, Weiwei Sun, *Member, IEEE*, Jialin Li, Ninghui Diao, and Zongyi He

***Abstract*— The land surface reflectance data are indispensable to generate many other land products. Global land surface reflectance data have been routinely produced from remote sensing sensors aboard different satellite platforms. However, the original data, especially the daily data, suffer from a large number of spatial gaps, which result from atmospheric contamination and instrument deficiencies. This seriously limits their further applications. Many composite products with less spatial gaps have been generated to solve the above problem, but they easily sacrifice their temporal resolutions of original data. Even worse, they cannot be directly implemented in realistic applications because of the noise and composite seams. This paper proposes a temporal–spatial reconstruction method (TSRM) to generate daily gapless and seamless land surface reflectance data. The TSRM integrates both temporal and spatial information for recovering different land cover types using three processing steps. First, spatial gaps are coarsely filled with multiyear weighted average (Step1). After that, all the gaps that are not filled in the first step are interpolated by using harmonic analysis of time series with true value constraint (Step2). Finally, the reconstructed results in the last step are seamlessly processed using the Poisson image editing method, and the seamless daily reflectance data set is generated (Step3). The Moderate Resolution Imaging Spectroradiometer reflectance data set (MOD09GA and MYD09GA) on two testing areas is selected to verify the performance of the proposed TSRM. Experimental results show that the TSRM has good performance with regard to maintaining the temporal and spatial integrity of the daily land surface reflectance data. Results on different testing sites also demonstrate that the TSRM preserves spectral integrity with clear seasonal trends for each spectral band.**

Manuscript received May 22, 2017; revised November 2, 2017 and January 20, 2018; accepted February 11, 2018. This work was supported in part by the NSFC-Zhejiang Joint Fund for the Integration of Industrialization and Informatization under Grant U1609203, in part by the Key Laboratory for National Geography State Monitoring (National Administration of Surveying, Mapping and Geoinformation) Open Fund under Grant 2016NGCM03, in part by the Chinese National Science Foundation under Grant 41671342 and Grant 41401389, in part by the Ningbo University Fund under Grant XYL17005, in part by the National High Technology Research and Development Program of China under Grant 2013AA12A301, and in part by the K. C. Wong Magna Fund in Ningbo University. *(Corresponding authors: Gang Yang; Huanfeng Shen.)*

G. Yang, W. Sun, and J. Li are with the Department of Geography and Spatial Information Techniques, Ningbo University, Ningbo 315211, China (e-mail: love64080@163.com; sunweiwei@nbu.edu.cn; lijialin@nbu.edu.cn).

H. Shen is with the School of Resource and Environmental Sciences and the Collaborative Innovation Center of Geospatial Technology, Wuhan University, Wuhan 430079, China (e-mail: shenhf@whu.edu.cn).

N. Diao is with the Beijing Remote Sensing Satellite Ground Station, National Satellite Ocean Application Service, Beijing 100086, China (e-mail: diaoninghui@mail.nsoas.org.cn).

Z. He is with the School of Resource and Environmental Sciences, Wuhan University, Wuhan 430079, China (e-mail: 837381190@qq.com).

Color versions of one or more of the figures in this paper are available online at http://ieeexplore.ieee.org.

Digital Object Identifier 10.1109/TGRS.2018.2810271

***Index Terms*— Harmonic analysis of time series (HANTS), MOD09, Moderate Resolution Imaging Spectroradiometer (MODIS), MODIS surface reflectance, Poisson image editing, time series.**

I. Introduction

CONTINUOUS and spatio-temporally complete remotely sensed time series play a key role in earth science research, especially in monitoring the climate change [1]–[4]. Currently, a large number of radiometric data derived from satellite sensors, e.g., NOAA Advanced Very High Resolution Radiometer (AVHRR), Terra/Aqua Moderate Resolution Imaging Spectroradiometer (MODIS), or SPOT VEGETATION, have been archived to record the climate information of the past 30 years. A series of land surface variables, e.g., the normalized difference vegetation index (NDVI) [5], the land surface temperature, the leaf area index, and the fraction of photosynthetically active radiation, has been derived from these radiometric data [6] and widely applied in global climate change research since the 1960s [3], [7]–[12]. However, current radiometric data have a drawback of spatio-temporal discontinuity due to the atmospheric contamination and instrument problems. The nonideal atmospheric conditions, i.e., cloud contamination, dust, and heavy aerosols, adversely affect the process of radiative transfer and bring about noise and gaps to radiometric data, especially the data with daily temporal resolution. This negatively affects downstream products and seriously hampers the progress of studies on global climate change. Therefore, it is in urgent need to find out an appropriate method to obtain the daily spatio-temporally continuous radiometric data [2], [13].

Many scholars have been developing algorithms for reducing noise and filling the gaps in remotely sensed time series. Shen *et al.* [14] comprehensively summarize main temporal-based method in the review work for reconstructing the missing information in remote sensing data. The compositing procedures give an over n-day time period representation of the data sets, and they are commonly used on the remotely sensed time-series data to reduce the impact of nonideal conditions and [15]. The maximum-value compositing (MVC) technique [16] was developed to reduce the noise of the AVHRR data, and a higher percentage of clear-sky data can be obtained [17]. Other compositing schemes, e.g., the maximum difference in red and near-infrared (NIR) reflectance, the maximum thermal radiance, the maximum surface temperature, the minimum red reflectance, and the minimum scan angle,

and their combinations [18], have also been presented to produce standard AVHRR and MODIS land products [19]–[21]. However, all the composite methods are carried out at the cost of reducing the temporal resolution of the remotely sensed time-series data. The composited products highly rely on the selected compositing criteria, and significant bidirectional effects and temporal biases usually exist [15], [22]–[24]. Even worse, the land surface reflectance data contain many low-quality pixels, seams, and gaps after the n-day MVC.

A number of methods based on temporal interpolation and filter were then developed for denoising or filling the gaps in the remotely sensed time-series data. These methods eliminate the noise in a single pixel of remote sensing time-series data and can be generally categorized into four types. The first types of methods are common and classical, and they filter the time-series data in sliding windows according to certain criteria. Typical examples are the best index slope extraction method [25], the adaptive Savitzky–Golay (SG) filter [26]–[28], the mean-value iteration filter [29], the changing-weight filter [30], and the iterative interpolation for data reconstruction method [31]. The second type is the function-based methods, with representative examples of asymmetric Gaussian (AG) [32] and double logistic (DL) methods [33]. The AG and DL methods have been combined with the adaptive SG filtering method and integrated into TIMESAT software to investigate time-series satellite data [27], [34]. The third type is the frequency domain-based methods, e.g., the Fourier transform [14], [35], the harmonic analysis of time-series (HANTS) method [36], the moving weighted harmonic analysis method [37], and the wavelet-based method [17]. The typical application of frequency domain-based methods is to denoise the remotely sensed time-series data [38]–[41]. The fourth type methods, e.g., the temporal–spatial filter [42], [43], the CACAO method [44], and the ecosystem curve fitting method [22], have been developed with the consideration of some special factors. Researchers have also proposed other methods focusing on retrieving albedo data based on the bidirectional reflectance distribution function (BRDF) model [1], [45], [46]. However, most of these methods change all the pixel values of the composited time-series data since most of the publicly available remotely sensed time-series data are composited. Furthermore, these methods were designed from envisaged concepts and their performance has not been verified in processing daily time-series data. To the best of our knowledge, few temporal methods have been developed for reconstructing the surface reflectance time-series data (e.g., the MODIS MOD09 product), let alone the data with daily basis.

In addition, several methods based on multitemporal spatio-temporal information were developed to fill the gaps of the remotely sensed data. For example, the classical temporal replacement method could remove clouds from different types of remote sensing images and fill the gaps by replacing the lost information with the reference data on the same region [47]–[51]. And the temporal learning model-based methods fill the gaps by establishing a mathematical model under the perspective of compressed sensing or sparse representation [52], [53]. These methods work well only for certain defined conditions, and the reference data must be carefully selected. Moreover, these methods cannot be used to generate time-series data with the daily basis.

So far, it is quite a challenging work to generate gapless and seamless daily surface reflectance data and no relevant methods are available for solving the problem. Faced by the challenges, a new attempt has been made in this paper to produce daily gapless and seamless surface reflectance data (MOD09GA and MYD09GA) in time series. This paper integrates the spatial and temporal information by three processing steps. First, the spatial gaps are filled with multiyear weighted average, and that provides initial values for the next step. After that, all the gaps remained unchanged after the first step are refilled by using HANTS with true value constraint, where the true values are recovered in each iterative procedure. Finally, the Poisson image editing is adopted to make the results seamless. We will introduce the MODIS surface reflectance data and analyze the condition of the test data in Section II-A. The proposed algorithm will be described in Section II-B, followed by the results and conclusions in Sections III and IV, respectively.

II. Data and Method

A. Study Sites and Data

MODIS is an important sensor equipped in Terra (originally known as EOS AM-1) and Aqua (originally known as EOS PM-1) satellites. The orbits of Terra and Aqua around the earth are timed, so that Terra passes from north to south across the equator in the morning and Aqua passes south to north over the equator in the afternoon. Their collected surface reflectance data products are named MOD09 and MYD09, respectively, and have seven spectral bands (620–670, 841–876, 459–479, 545–565, 1230–1250, 1628–1652, and 2105–2155 nm). The data have been corrected for the effects of gaseous and aerosol scattering and absorption as well as adjacency effects caused by variation of land cover, BRDF and atmosphere coupling effects, and contamination by thin cirrus [54]. The associated data state quality assessment (QA) stored in the data [55] quantifies the quality of these data, whether the pixel has been flagged as land, deep ocean, shallow ocean, or as containing cloud, high aerosol, low aerosol, snow, or fire [56]. The important information helps users to know about the quality of the MODLAND products.

The daily MOD09GA and MYD09GA data at 500-m spatial resolution on two different test areas have been chosen to evaluate our algorithm in constructing daily MODIS surface reflectance data. In Fig. 1, the data set (112.9–115.4°E, 30.1–32.3°N) of first area was extracted from the MYD09GA data of the year 2011. The area is located in mid-southern China covering all the Wuhan city and part of Hubei province and enjoys a subtropical humid monsoon climate with plenty of sunshine and ample rainfalls. The area is mostly covered by clouds all the year round, and the corresponding daily MODIS data seriously suffer from information loss. The second test area has a subset (97.5–101.1°E, 37.6–39.8°N) of the MOD09GA data of the year 2011. Its area in Fig. 1 is located in northwestern China covering most of Zhangye city in

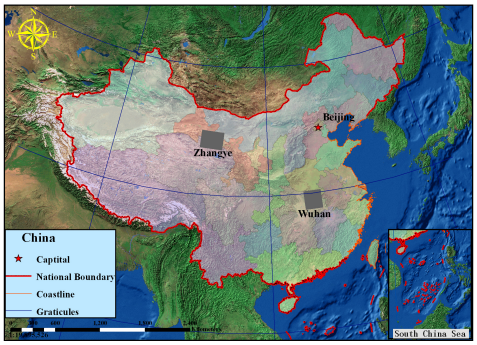

Fig. 1. Locations of the two test areas in China. Wuhan is located in mid-southern China within a subtropical humid monsoon climate, and Zhangye is located in northwestern China within a continental windy and dry climate.

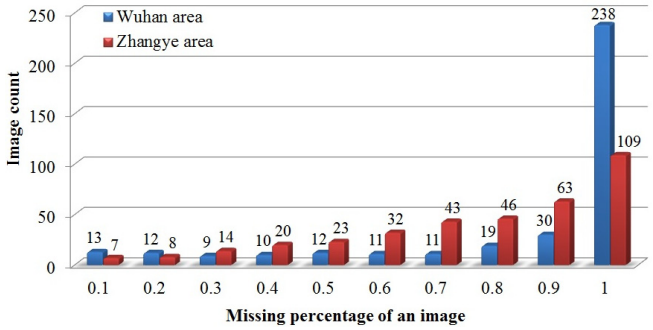

Fig. 2. QA of the test data in 2011. The horizontal axis represents the missing percentages of each image according to QA information, and the vertical axis counts the total number of images of different missing percentages.

TABLE I
LAND COVER TYPES OF THE TWO TEST AREAS

Area	Land cover type
Wuhan	needle leaved evergreen forest, broadleaved deciduoud forest, bush, slope grassland, city, river, swamp, farmland
Zhangye	needle leaved deciduoud forest, bush, alpine and sub-alpine meadow, desert grassland, meadow, lake, glacier, gravels, bare rocks

Gansu province. The continental windy and dry climate leads to less cloud coverage than Wuhan area. Different climates result in different land cover types of the two test areas. Table I shows detailed land cover types of the two areas, where the types are referred from the Global Land Cover 2000 Project data. The two test areas have multiple land cover types and different cloud coverage conditions, and they can be good candidates to evaluate our proposed method.

Four preprocessing works are required for these data to ensure the successful operation of the test experiments. First, the bad-quality, high-aerosol, cloudy, and cloud-shadow MODIS observations will be masked with the help of QA information. Second, the abnormally high values in each band are eliminated by threshold judgment. Third, we assume that the remaining pixels after masking are applicable, and part of the applicable pixels with true values will be masked randomly by different percentages, and the masked pixels are set as the simulated missing observations. Within this step, a number of pixels are generated randomly in the study area, and buffers with 10 pixels as the radius are generated for these pixels. The intersection of these buffers with applicable pixels is the simulated missing part. The simulated missing observations are used to carry out the quantitative assessment. All these simulated masked pixels will be reconstructed by our proposed method. Finally, the mask file for each band of all the test data will be generated by combining the QA information with the simulated missing pixels to help identifying the missing pixels. The details of above processes and the data condition analysis will be described in Section III. In addition, we recalculate the pixel value to the normal value range of 0–1 by dividing the pixel value by 10 000. The resulting pixel values that are larger than 1 are set to be 1 and those less than 0 are set to be 0. There are 365 datasets for each test area in 2011, and each dataset with seven bands is encountered with different percentages of missing pixels. Using the QA information, we mask these missing pixels with bad quality, high aerosol, cloudy, and cloud shadow. A quantitative statistic for the masked pixels of each image will be given to assess the quality of data. As shown in Fig. 2, the horizontal axis represents the missing percentage of each image according to QA information, and we divide it into 10 equal parts, each of which is 0.1. The vertical axis represents the quantity of images located in these parts. For Wuhan area, 238 images over 90% of the information were missing. This means that this area is covered by high cloud all the year round. The Zhangye area is less affected by cloud cover than is Wuhan area. A total of 109 images lack over 90% of the information, and 60% of the test data lack over 70% of the information. More seriously, there is a big probability that the single-pixel time-series data are successively missing, which makes temporal filter methods unable to cope with this situation. The temporal–spatial reconstruction method (TSRM) is proposed to address the challenge, and its detailed demonstration will be provided in Section II-B.

B. Methodology

Fig. 3 illustrates the flowchart of the TSRM in generating spatio-temporally complete daily MODIS surface reflectance data. The gradual process includes three main steps: 1) the determination of the background information (Step1); 2) the intra-annual temporal interpolation (Step2); and 3) the post-processing for seamless data (Step3). Step1 aims to estimate the background information for Step2 by multiyear weighted average, where the normalization processing is required. Step2 fills the gaps of the images remained after Step1 by using HANTS with true value constraint. Step3 implements the postprocessing work in the results of Step2, where the Poisson image editing method is used to adjust all reconstructed pixel values to ensure the seamless results.

1) Step1 (Determination of the Background Information): In this step, the background information is first calculated using the multiyear weighted average, and it is very essential to the temporal interpolation process in Step2. The moment matching algorithm [57] is introduced herein to normalize the data. Assuming that the images across different years

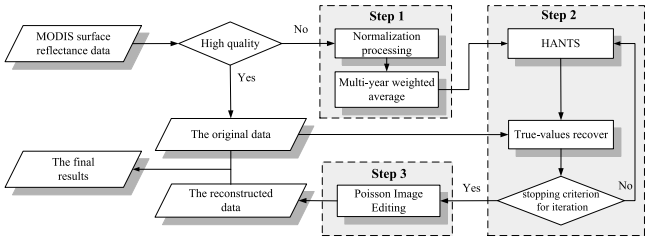

Fig. 3. General process of the TSRM.

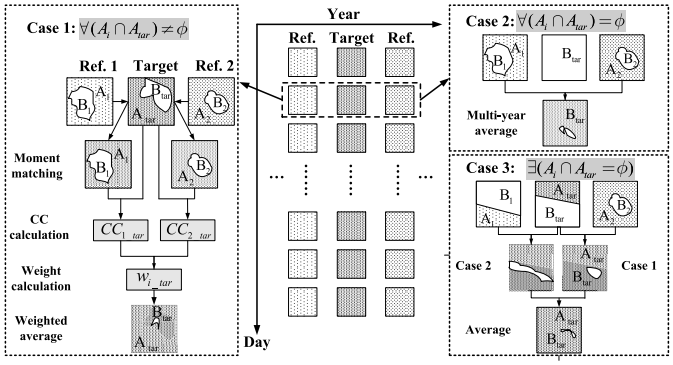

Fig. 4. Schematic of Step1. The schematic of the intermediate position represents three years of simulated experimental data. Target and Ref. represent the time-series data that need reconstructing and the reference time-series data, respectively. (Left and Right) Schematic of three situations that need to be considered in the reconstruction process.

contain a statistically similar subscene, the algorithm examines the distribution of pixel values in the image for different years and adjusts the distribution to that of pixel values in the reference image. Actually, if the land cover does not vary dramatically across different years, the linear correlation between multitemporal data is significant. Accordingly, we only adjust the average values and the standard deviations between each image and the reference image [57]. The correlation coefficients (CCs) [58] between the target images (i.e., the time-series data that require reconstructing) and the reference images (i.e., the multiyear reference data) will be calculated to estimate the weight of the reference data. This process is carried out with the consideration of the interannual variation and the spatial information of the images, and we will comprehensively explain it with the combination of the schematic in Fig. 4.

When implementing this step on the MODIS surface reflectance data, three cases should be taken into account. Take three years of simulated data as an example to explain the schematic in Fig. 4, where Target is the time-series data that need reconstructing, and Ref. is the reference time-series data, which are the multiyear time-series data in our experiments. The horizontal axis represents the year when the time-series data were collected, and the vertical axis denotes one day of the year. These data have been preprocessed using the QA information. In the diagram, A_i and A_{tar} represent the availability areas with applicable pixels of the reference data and the target data, respectively. B_i and B_{tar} represent the masked areas with low-quality pixels of the reference data and the target data, respectively. The detailed description is as follows.

Case ① [$\forall(A_i \cap A_{tar}) \neq \phi$]: It means that there are overlapping availability areas between the reference data and the corresponding target data. First, the reference data will be adjusted by using the moment matching algorithm described as

$$g^i_{\text{adj}} = \left(g^i_{\text{ref}} - \mu^i_{\text{ref}}\right)\frac{\sigma_{\text{tar}}}{\sigma^i_{\text{ref}}} + \mu_{\text{tar}} \tag{1}$$

where g^i_{adj} is the adjusted pixel value, and g^i_{ref} and μ^i_{ref} represent the ith year's pixel value and mean value of the overlapping availability areas of the reference data, respectively. μ_{tar} is the mean value of the overlapping availability area of the target data, σ^i_{ref} is the ith year's standard deviation of overlapping availability areas of the reference data, and σ_{tar} is the standard deviation of the overlapping availability area of the target data.

After that, pixel values of all the reference data have similar distribution to those of the corresponding target data. The Pearson CC of the overlapping availability areas are calculated using the metric defined as

$$\text{CC}^i_{\text{adj\_tar}} = \frac{\sum_{j=1}^{n}\left(g^i_{\text{adj}(j)} - \overline{g^i_{\text{adj}}}\right)\left(g^i_{\text{tar}(j)} - \overline{g^i_{\text{tar}}}\right)}{\sqrt{\sum_{j=1}^{n}\left(g^i_{\text{adj}(j)} - \overline{g^i_{\text{adj}}}\right)^2 \sum_{j=1}^{n}\left(g^i_{\text{tar}(j)} - \overline{g^i_{\text{tar}}}\right)^2}} \tag{2}$$

where n is the total number of the overlapping availability area pixels, $g^i_{\text{adj}(j)}$ and $g^i_{\text{tar}(j)}$ are the adjusted reference and target pixel values, respectively, and $\overline{g^i_{\text{adj}}}$ and $\overline{g^i_{\text{tar}}}$ are the mean value of the adjusted reference data and the target data, respectively. A larger CC indicates the closer similarity between the two groups of values.

With the CC, the weight of all the adjusted reference pixels can be calculated using the following equation:

$$w^i_{\text{adj}(j)} = \begin{cases} 0, & \forall p^i_{\text{ref}(j)} = 0 \\ \dfrac{p^i_{\text{ref}(j)}\text{CC}^i_{\text{adj\_tar}}}{\sum_{i=1}^{m} p^i_{\text{ref}(j)}\text{CC}^i_{\text{adj\_tar}}}, & \text{others} \end{cases} \tag{3}$$

where $w^i_{\text{adj}(j)}$ is the weight of the jth pixel of the ith year reference data, m is the number of years of the reference data, and $p^i_{\text{ref}(j)}$ is the corresponding quality flag defined as 1 or 0 when the pixel is applicable and inapplicable, respectively. $\forall p^i_{\text{ref}(j)} = 0$ means that if all the pixels at the same location of different years are flagged as 0 simultaneously, the corresponding weights of all the pixels are 0.

Finally, we fill the missing areas of the target data by multiyear weighted average defined as

$$g_{\text{tar}(j)} = \sum_{i=1}^{m} w^i_{\text{adj}(j)} g^i_{\text{adj}(j)} \tag{4}$$

where $g_{\text{tar}(j)}$ is the jth reconstructed pixel value in the missing areas of the target data.

Case ② [$\forall(A_i \cap A_{tar}) = \phi$]: It means that there is no overlapping availability area between the reference data and the corresponding target data. The moment matching algorithm

and the Pearson CC are not appropriate in this case. The missing areas of the target data will be filled by the simple multiyear average of the reference data using the following equation:

$$g_{\mathrm{tar}(j)} = \begin{cases} 0, & \forall p^i_{\mathrm{ref}(j)} = 0 \\ \dfrac{\sum_{i=1}^{m} p^i_{\mathrm{ref}(j)} g^i_{\mathrm{ref}(j)}}{N}, & \text{others} \end{cases} \tag{5}$$

where m is the number of years of the reference data, $p^i_{\mathrm{ref}(j)}$ is the quality flag, and N is the total number of the reference pixels with p equal to 1 at the same location for different years.

Case ③ [$\exists(A_i \cap A_{tar} = \phi)$]: This case is the combination of case ① and case ②. We first separate it into case ① and case ② and then fill the missing area of the target data according to the rules in case ① and case ②. Case ① and case ② produce a separate value, and we obtain the multiyear average for case 3 by averaging the two values

$$g_{\mathrm{tar}(j)} = \begin{cases} 0, & p_{\mathrm{ca1}(j)} = 0 \parallel p_{\mathrm{ca2}(j)} = 0 \\ \dfrac{p_{\mathrm{ca1}(j)} g_{\mathrm{ca1}(j)} + p_{\mathrm{ca2}(j)} g_{\mathrm{ca2}(j)}}{p_{\mathrm{ca1}(j)} + p_{\mathrm{ca2}(j)}}, & \text{others} \end{cases} \tag{6}$$

where $g_{\mathrm{ca1}(j)}$ and $g_{\mathrm{ca2}(j)}$ are the jth pixel values of the results from case ① and case ②, respectively. $p_{\mathrm{ca1}(j)}$ and $p_{\mathrm{ca2}(j)}$ are their corresponding quality flags. It is 1 if the missing area is filled; otherwise, it is 0.

2) Step2 (Intraannual Temporal Interpolation): The process in Step1 can only fill the gaps coarsely. The results still contain gaps when the reference data values are missing over all the years. Accordingly, we adopt the HANTS algorithm in pixel level based on the intra-annual temporal information, in order to fill the gap thoroughly.

The HANTS algorithm was developed based on the Fourier transform and has been widely used to reconstruct time series of remotely sensed quantitative products during the past 20 years. Its reconstruction mechanism is to remove random noise caused by atmospheric contamination and instrument problems. Its mathematical expression can be represented as the sum of a constant and the superimposed sequence of sines and cosines [2], [37], given by

$$\tilde{g}(t) = a_0 + \sum_{k=1}^{nf} [a_k \cos(2\pi f_k t) + b_k \sin(2\pi f_k t)] \tag{7}$$

$$g(t) = \tilde{g}(t) + \varepsilon(t), \quad t = 1, \ldots, N \tag{8}$$

where g, $\tilde{g}$, and ε are the original time series, the reconstructed series, and the error series, respectively. t is the time note of g, and N is the length of the time series. a_k and b_k are the coefficients of the trigonometric components with the frequencies f_k, and nf is the number of harmonics associated with the frequencies f_k.

The HANTS algorithm is an iterative process with the specific steps described as follows.

1) Reject the pixels outside the valid range of data. For example, the valid range for land surface reflectance can be 0–1, and the pixels out of this range will be rejected.
2) Fit the remaining valid pixels by solving the equations above using the least-squares method.
3) Repeat the algorithm until the condition satisfies. The condition is defined as follows: maximum error between the current curve and the input data is smaller than the given threshold, or the number of remaining pixels is not enough for the reconstruction process.

TABLE II
PARAMETER SETTINGS OF HANTS WITH TRUE VALUE CONSTRAINT IN THIS PAPER

Parameters	Description	values
NI	Number of samples of one base period	365
NF	Number of frequencies	10
Hilo	The suppression flag indicating whether high or low values should be rejected during curve fitting	None
low	Low threshold	0
high	High threshold	1
FET	Fit error tolerance	0.05
DOD	Degree of overdeterminedness, which is a safety measure assuring the number of valid observations is greater than or equal to the necessary minimum.	5
Delta	Damping factor, which is a small positive number to suppress high amplitudes	0.5

In order to make the reconstructed time-series approach to the original ones, we adopt the true value constrain strategy. The strategy is to recover the original value that was not masked by the QA information after fitting the remaining valid pixels. It should be noted that the simulated masked true values mentioned in the preprocessing are used only for validation purposes and do not participate in the development of the algorithm for the pixels masked by QA information.

It should be noted that several parameters have to be set carefully when implementing the algorithm. It has been pointed out that no objective rules are available to determine these parameters [38]. Considering that the aim here is to roughly fill the gaps of the time-series data, we set the parameter "Hilo" as "none," and set the parameter "number of frequency (NF)" experimentally. The other parameters are set by referring to some previous applications from others. The detailed parameter settings are shown in Table II. Zhou *et al.* [2] have given a general evaluation of the reconstruction performance using the 16-day composite NDVI time series, where the NF is set as 4. Different from the 23 samples in an annual series, 365 samples with higher frequencies (higher than 4) are required to fit the curve reasonably, just as Moody and Johnson [59] argued that only with higher frequencies can the fitting captures high temporal variability. In order to give a more acceptable performance of HANTS, we experimentally set the NF as 10 in the study. The fit error tolerance was set as 0.05 (the MODIS surface reflectance unit) experimentally in consideration of balancing the efficiency and accuracy of the algorithm. The damping factor is set as 0.5 [2]. The degree of overdeterminedness (DOD) is set as 10 in order to ensure that the valid observations satisfy

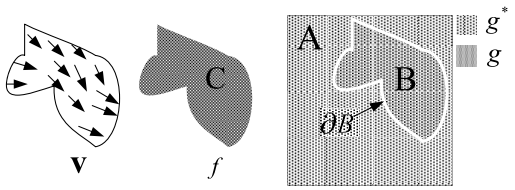

Fig. 5. Guided interpolation notations. Unknown function g interpolates in domain B with the destination function g^*, under guidance of vector field $\mathbf{v}$, which is the gradient field of a source function f.

the necessary minimum. The valid range of land surface reflectance is between 0 and 1. It should be noted that the damping factor and DOD will not affect the reconstruction results basically, and the parameter settings are empirical and universal for the daily reflectance product reconstruction.

3) Step3 (Postprocessing for Seamless Data): By using the HANTS algorithm, we obtain better spatio-temporal continuous time-series data. Unfortunately, some seams still exist at the boundary between the good areas and the reconstructed areas. The seamless editing is then necessary, and we introduce the interpolation machinery based on Poisson equations to achieve the purpose. The key point of the algorithm is the Poisson partial differential equation under Dirichlet boundary conditions. These conditions specify the Laplacian of an unknown function over the domain of interest, along with the unknown function values over the boundary of the domain [60]. It is a minimization problem in the L_2-norm to solve the Poisson equation, which computes the function whose gradient is closest to some prescribed vector field under the given boundary conditions. For convenience, Fig. 5 illustrates the notations: B is a closed subset of $A + B$ with boundary ∂B. g is an unknown scalar function defined over the interior of B. g^* is a known scalar function defined over A. $\mathbf{v}$ is the guidance of the vector field of a source closed subset C with function f.

The requirement of image merging is to make the merged image look as smooth as possible without obvious boundaries. Therefore, the interpolant g of g^* over B is defined as minimizing the following problem:

$$\min_g \iint_B |\nabla g|^2 \quad \text{s.t. } g|_{\partial B} = g^*|_{\partial B} \tag{9}$$

where $\nabla . = [(\partial ./\partial x), (\partial ./\partial y)]$ is the gradient operator. The minimizer must satisfy the associated Euler–Lagrange equation defined as

$$\Delta g = 0 \quad \text{s.t. } g|_{\partial B} = g^*|_{\partial B} \tag{10}$$

where $\Delta . = (\partial^2./\partial x^2) + (\partial^2./\partial y^2)$ is the Laplacian operator. However, the solution obtained by (10) does not contain the information of the source image. In order to guarantee the merged image in B close to source image C, we introduce further constraints in the form of a guidance field as explained below.

Here, we used the gradient field $\mathbf{v}$ of f as the guidance field, and the extended equation is described as

$$\min_g \iint_B |\nabla g - \mathbf{v}|^2 \quad \text{s.t. } g|_{\partial B} = g^*|_{\partial B}. \tag{11}$$

The minimizer must satisfy the associated Euler–Lagrange equation, and the unique solution follows the Poisson equation with Dirichlet boundary conditions:

$$\Delta g = \text{div}\mathbf{v} \quad \text{s.t. } g|_{\partial B} = g^*|_{\partial B} \tag{12}$$

where $\text{div}\mathbf{v} = (\partial u/\partial x) + (\partial v/\partial y)$ is the divergence of $\mathbf{v} = (u, v)$. This is the fundamental machinery of Poisson editing: seven Poisson equations of the form (12) are solved independently in seven bands of the chosen data.

This step is applied to all the reconstructed images because of the inevitable existence of the seams on the boundary between the reconstructed area and the original area. The mask files are used to determine which images need to be handled in this step. They are generated in the preprocessing steps in accordance with the size of the original image. Their pixel values are composed of two values, where the value of reconstructed area is assigned to 1 and the value of original area is assigned to 0. If all the values of the mask file are 1 or 0, its corresponding image does not need to carry out this step. When this step is performed on the reconstructed image, the 0 and 1 transition places are the boundary and where the seam exists. So the boundary and seams can be identified according to the mask files.

In this step, B is the reconstructed area obtained by HANTS with true value constraint. The pixel values of the area need to be corrected. $\mathbf{v}$ is the gradient field calculated based on guidance area C. This area does not need to have a true value, but it must have effective gradient information. We can obtain the intermediate product after HANTS before true value constraint in Step2. Although the pixel value of the intermediate product cannot represent the true value, it has the approximate correct gradient information. So the guidance field $\mathbf{v}$ is calculated based on the intermediate product. In conclusion, this step adjusts the pixel values of the whole reconstructed area, not only smoothing the boundaries in the image under the guidance of gradient and Dirichlet boundary conditions.

III. Results

The TSRM described in Section II is employed to generate spatio-temporally complete MODIS land surface reflectance data. This is accomplished by analyzing one year's data of the MOD09GA (MYD09GA) data from Terra (Aqua) on two test areas. For the Wuhan area, we selected the MYD09GA data in 2009, 2010, and 2012, as the reference data. This ensures sufficient initial values for temporal interpolation (Step2). For the Zhangye area, the MOD09GA data in 2010 and 2012 were selected as the reference data. Sections III-A and III-B detail both the qualitative and quantitative assessments of this new method.

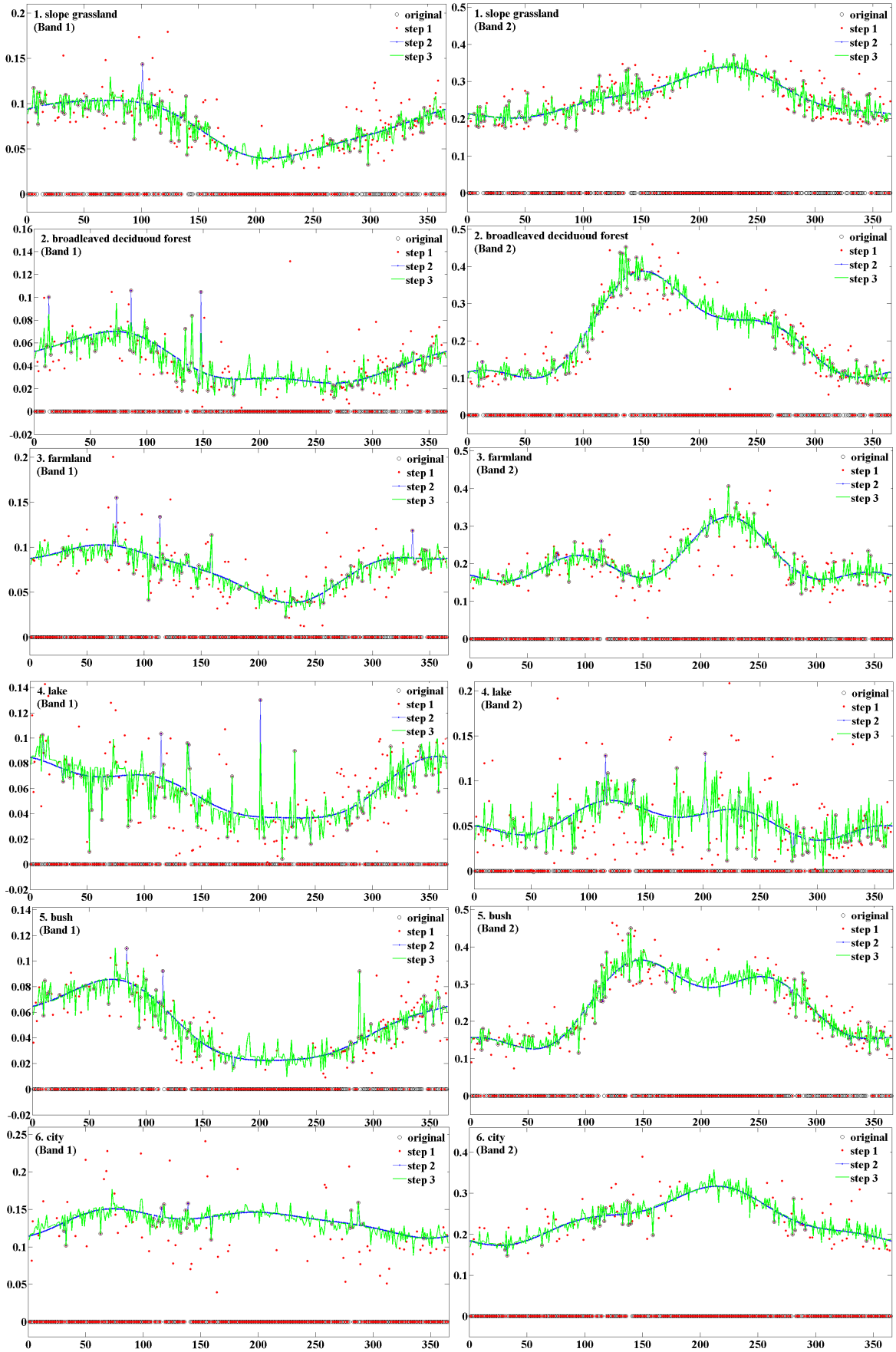

Fig. 6. Results of the reconstructed MODIS surface reflectance time-series data on two spectral bands (band 1 and band 2) generated by each step of TSRM.

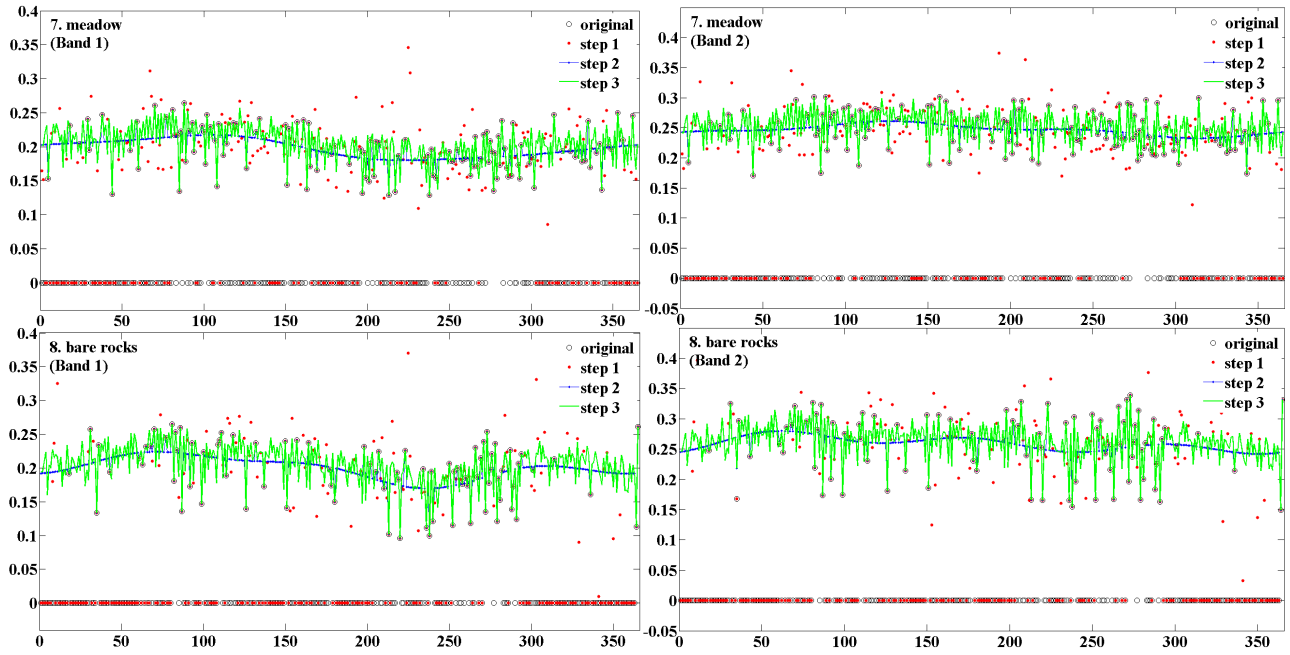

Fig. 6. *(Continued.)* Results of the reconstructed MODIS surface reflectance time-series data on two spectral bands (band 1 and band 2) generated by each step of TSRM.

TABLE III
VEGETATION TYPE OF TEST POINTS

Test point	Test area	Vegetation type	Test point	Test area	Vegetation type
1	Wuhan	slope grassland	5	Wuhan	bush
2	Wuhan	broadleaved deciduoud forest	6	Wuhan	city
3	Wuhan	farmland	7	Zhangye	meadow
4	Wuhan	lake	8	Zhangye	bare rocks

A. Qualitative Assessment

Certain criteria have been established to evaluate the reconstruction effectiveness of the proposed method. Among them, the qualitative assessment is commonly used in the comparison of alternative reconstruction methods, since ground truth of the MODIS surface reflectance time series cannot be obtained. In this section, we undertook a visual inspection for the qualitative assessment from two aspects. First, we selected several test pixels to plot their results for each step of the proposed method. And then, the demonstration of the reconstruction process for local regions was applied to illustrate the effectiveness of the new method.

1) Single Pixel Time-Series Demonstration: We selected 200 test pixels randomly from the two test areas with different land cover types to demonstrate the reconstruction process of our proposed method. Due to the space limitations, we just show the results of eight test pixels corresponding to vegetation types in Table III. Meanwhile, the visual inspection of the original, intermediately processed, and the final reconstructed time-series data obtained from the new proposed method gives a preliminary qualitative assessment. Specifically, we plotted two spectral bands (band 1 and band 2) time series of the selected eight test pixels.

Fig. 6 shows the results of reconstructed MODIS surface reflectance time-series data in pixel level of band 1 and band 2. The results of each step are also shown to demonstrate the reconstruction process. The selected eight test pixels with different land cover types were used to show the results typically. All the information obtained from the results can be explained mainly from three aspects. First, the MOD09GA and MYD09GA data with daily temporal resolution are with high cloud coverage, which causes the information loss. Most of original data in Fig. 6 have the pixel value of 0, which indicates the high proportions of missing pixels. Particularly, the Wuhan area has higher cloud coverage than does the Zhangye area. Much of the successive information missing makes it difficult to construct the missing pixels using the general temporal filtering method that only utilizes the temporal information. Second, the QA information can correctly identify most of the pixels that are contaminated by cloud, high aerosol, or snow. Finally, the original surface reflectance time-series data are with some regular fluctuations, as shown by test pixels 7 and 8. The general variation profiles of the reconstructed surface reflectance time-series data show that the proposed method can fill the missing information correctly with regular fluctuations of the time series.

For each step of the proposed method, Step1 is essential to calculate the initial values for the temporal interpolation of Step2 by averaging the multiyear information. However, the missing information is not filled completely via Step1. The red asterisks in Fig. 6 illustrate the results generated by Step1, and most of them are 0 due to the simultaneously missing of multiyear information at the same location. In Step2, we used a modified HANTS method to fit the pixels retained

via Step1. The blue lines with asterisk in Fig. 6 show the smooth profiles of the land surface reflectance time-series data. It is convincing that the temporal continuous data were generated via Step2. Some correction works have been done on the atmosphere effects and the adjacency effects caused by variations in land cover type, BRDF, and the atmosphere coupling effects, but these residual effects on the surface reflectance still exist [61]. Therefore, it is impossible for the real surface reflectance time series to show such a smooth profile without any fluctuations [62]. The smooth profile only indicates the main growing trend of the land cover type rather than the real profile of the time series. In this condition, some adjustments are required to make the reconstructed time-series approach to the real profiles. Step3 is the right solution strategy to adjust the filtered results based on the spatial information. The green lines with solid dots in Fig. 6 indicate that the final results after the Poisson image editing own a general profile with seasonal variations and have some regular fluctuations along the growing trend.

Most of the eight test pixels were selected with different land cover types. The first six test points were selected from Wuhan area while the other two pixels were selected from Zhangye area. For the test pixels 1, 2, 3, and 5, band 2 (841–876 nm, NIR) clearly displays a seasonal growing trend with high values in summer period because the chlorophyll has high reflectivity in the NIR region. Band 1 (620–670 nm, red) corresponds to one of the main absorption wavelengths of chlorophyll (430–450 and 650–660 nm). Fig. 6 shows reasonable results of these four test pixels on band 1, where the valley values exist in summer period. The test pixels 7 and 8 are located in dry regions with few vegetation covers. The time-series profiles illustrate a stable tendency all the year round on all the seven bands. Test pixel 4 has a nearly seasonal change trend with low values all the year round on bands 1 and 2. The explanation for this is that water with phytoplankton has low reflectivity in red and NIR regions. For test pixel 6, bands 1 and 2 show the stable change curves with less obvious seasonal pattern. The reason for this is the spatial homogeneity of underlying surface characteristics. The aforementioned analysis of the results indicates that the TSRM can successfully reconstruct the missing information meanwhile preserving the integrity of the phenology.

2) Demonstration for Local Regions: To further demonstrate the gradual reconstruction process and test the effectiveness of the TSRM at a regional scale, we show the examples of the original MODIS surface reflectance values and the intermediate results of TSRM MODIS surface reflectance values in each processing step. Considering the space limitations, we only show the results of MODIS true-color combination (bands 1, 4, and 3) of the two test areas. There are many unnatural colors appearing in the true-color combination images, as shown by the red/pink points in Fig. 7 and the red points in Fig. 8. The reason is that the abnormally high values exist in different locations of the seventh band image.

Fig. 7 shows the results of Wuhan area on May 12, 2011, which is right in the vegetation growing season. Fig. 7(a) shows the original MODIS land surface reflectance data, where the bad-quality, high-aerosol, cloudy, cloud-shadow, and

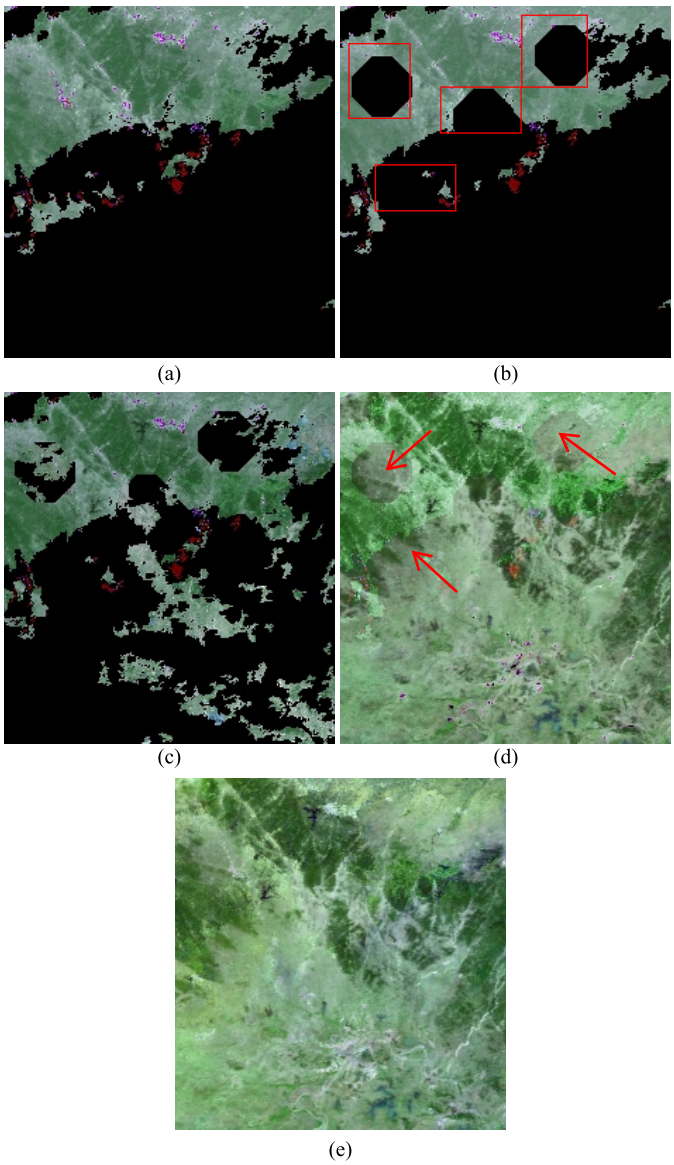

Fig. 7. MODIS true-color combination results for Wuhan area. (a) Original image. (b) Simulated missing image. (c) Step1 results. (d) Step2 results. (e) Step3 results.

the abnormally high-value observations were masked using the QA information and the threshold judgment. Fig. 7(b) illustrates the simulated missing data based on Fig. 7(a). The red rectangle in Fig. 7(b) covers some applicable pixels, and they are manually masked for the further quantitative assessment. Fig. 7(c) shows the result of Step1 that is obtained from gap filling with the multiyear weighted average values. Only a small part of the gaps can be filled because the high cloud coverage causes the inadequate information across the multiyears. Fig. 7(d) shows the results derived from Step2. Almost all the gaps were successfully filled, but some seams directed by the red arrows in Fig. 7(d) still appear clearly at the boundary between good areas and the reconstructed areas. The land surface with the same land cover type displays inconsistent color between good areas and the reconstructed areas. Fig. 7(e) explains the seamless results after the Poisson

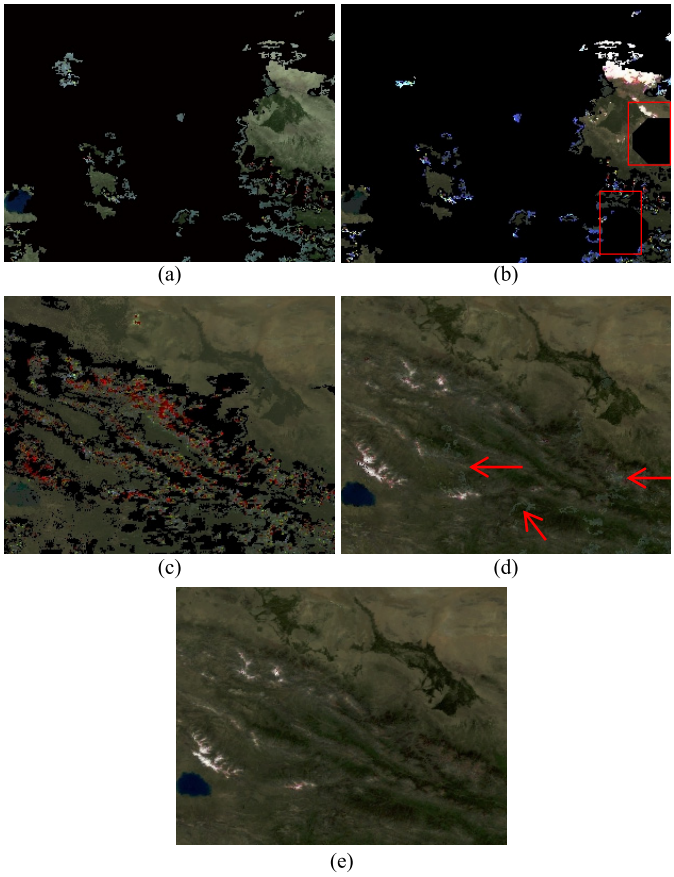

Fig. 8. MODIS true-color combination results for Zhangye area. (a) Original image. (b) Simulated missing image. (c) Step1 results. (d) Step2 results. (e) Step3 results.

image editing in Step3. Almost all the seams have been removed, and the land surface objects show normal colors in the true-color combination image.

Fig. 8 shows the results of Zhangye area on August 2, 2011, which is the summer of the year. Fig. 8(a) shows that this area has high cloud coverage on the day. But it has relatively low cloud coverage on the same day of the adjacent years, and Fig. 8(c) shows that most of the gaps have been filled after the multiyear weighted average. The remaining gaps were filled after the temporal interpolation, and the generated nearly spatio-temporal continuous data are shown in Fig. 8(d). Fig. 8(d) also show some seams which are caused by spectrum distortion, and they are completely removed [shown in Fig. 8(e)] after Poisson image editing. The Zhangye area has better reconstruction results than does Wuhan area, and the reason is simplicity and strong consistency of the land cover type in Zhangye area.

In addition, the original and reconstructed MODIS true-color combination time-series images on the two test areas are displayed to demonstrate the effectiveness of the reconstructed results. We selected the images on the 10th and 20th days of each month for Wuhan area and Zhangye area, respectively. Figs.9(a) and 10(a) show the original MODIS true-color combination time-series images of Wuhan area and Zhangye area, respectively. Most of the images suffer from cloud and other contaminations, and these data cannot be directly used in further applications. The results from TSRM on the two test areas are shown in Figs. 9(b) and 10(b). Visually, all the information in the cloud coverage area is effectively reconstructed.

TABLE IV

TOTAL QUANTITATIVE ASSESSMENT COMPARISON OF THE RESULTS OBTAINED AFTER STEP2 AND STEP3 OF THE NEW METHOD

		Wuhan area		Zhangye area	
		Step 2	Step 3	Step 2	Step 3
CC	Band1	0.8128	**0.9407**	0.8696	**0.9550**
	Band2	0.8536	**0.9648**	0.8287	**0.9461**
	Band3	0.7861	**0.9103**	0.8065	**0.9122**
	Band4	0.7281	**0.9375**	0.8016	**0.9297**
	Band5	0.7688	**0.9555**	0.7768	**0.9186**
	Band6	0.6558	**0.9186**	0.8523	**0.9513**
	Band7	0.7640	**0.9382**	0.8985	**0.9627**
RMSE	Band1	0.0161	**0.0088**	0.0305	**0.0178**
	Band2	0.0347	**0.0175**	0.0347	**0.0195**
	Band3	0.0086	**0.0057**	0.0227	**0.0147**
	Band4	0.0137	**0.0068**	0.0307	**0.0185**
	Band5	0.0383	**0.0177**	0.0427	**0.0268**
	Band6	0.0368	**0.0192**	0.0401	**0.0237**
	Band7	0.0265	**0.0142**	0.0371	**0.0229**
ARE	Band1	0.1904	**0.0938**	0.1742	**0.0876**
	Band2	0.1344	**0.0634**	0.1313	**0.0641**
	Band3	0.1896	**0.1187**	0.2265	**0.1287**
	Band4	0.1506	**0.0702**	0.2028	**0.0977**
	Band5	0.1467	**0.0671**	0.1276	**0.0691**
	Band6	0.1755	**0.0898**	0.1205	**0.0641**
	Band7	0.1943	**0.1009**	0.1363	**0.0794**

Vegetation cover is also the best indication to reflect the temporal variations of the ground truth. The vegetation in different climates and different places shows different temporal variations. For the Wuhan area in Fig. 9(b), the temporal variations of vegetation coverage are not obvious. The explanation for that is the sufficient sunshine and ample rainfalls in subtropical humid monsoon climate of Wuhan area brings about the lush vegetation. Specifically, the mixed broadleaf evergreen and deciduous forest dominates in the mountains, and the vegetation variations in mountains are insignificant. Some temporal variations exist in plain areas, where the crops grow from seeding to harvesting as the season changes. Fig. 10(b) shows the clear temporal variations of vegetation coverage appear in Zhangye area. This area enjoys a continental climate with the characteristics of drying, less rain, windiness, cold, and long sunshine hours. The vegetation coverage varies greatly among different seasons. The snow cover in this area also displays apparent variations from accumulating to melting as the season changes. In a word, it shows good consistence between these time-series results and the ground truth.

In general, the new proposed method improved the quality of the original data visually. Actually, the result of Step2 can be viewed as the results generated by the HANTS algorithm. So we can conclude that the proposed method can improve the results of the HANTS algorithm that is a representative method among the temporal filtering methods.

B. Quantitative Assessment

In this section, the quantitative assessment is implemented to further assess the TSRM algorithm. We made simulated

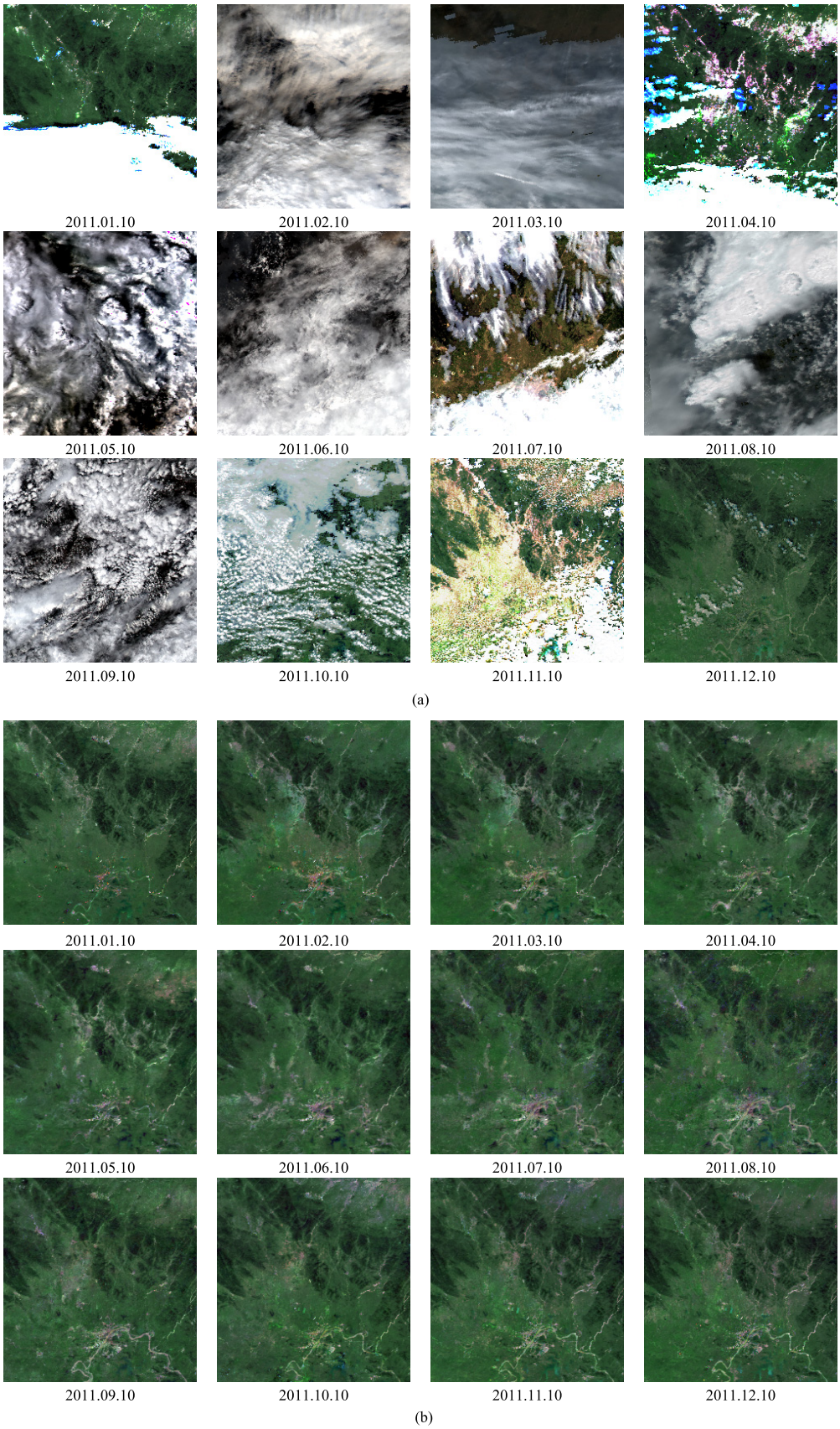

Fig. 9. Original and reconstructed MODIS true-color combination time-series images of Wuhan area (the images are selected on the 10th of each month in 2011). (a) Original MODIS true-color combination time series of Wuhan area. (b) Reconstructed MODIS true-color combination time series of Wuhan area.

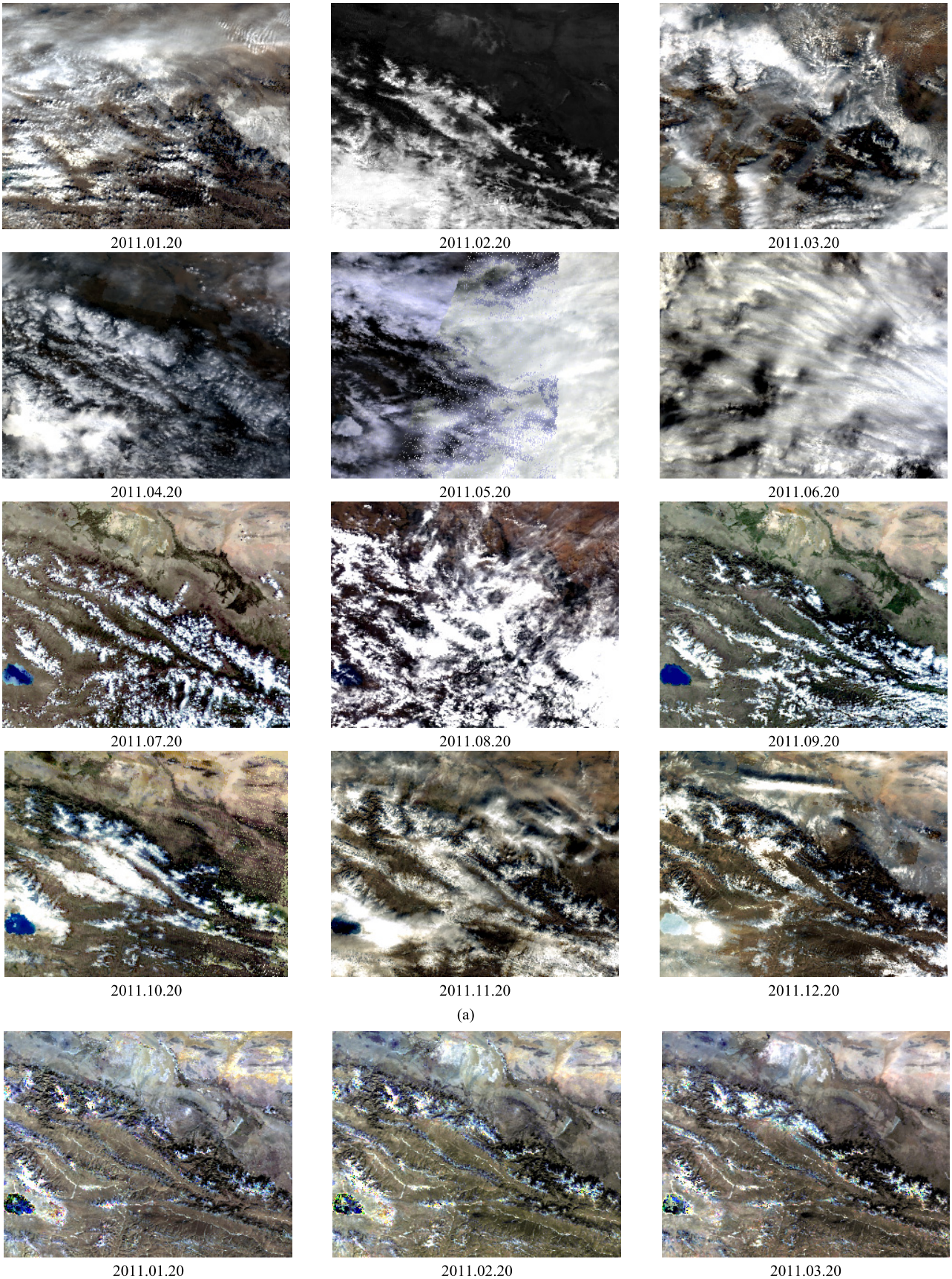

Fig. 10. Original and reconstructed MODIS true-color combination time-series images of Zhangye area (the images are selected on the 20th of each month in 2011). (a) Original MODIS true-color combination time series of Zhangye area. (b) Reconstructed MODIS true-color combination time series of Zhangye area.

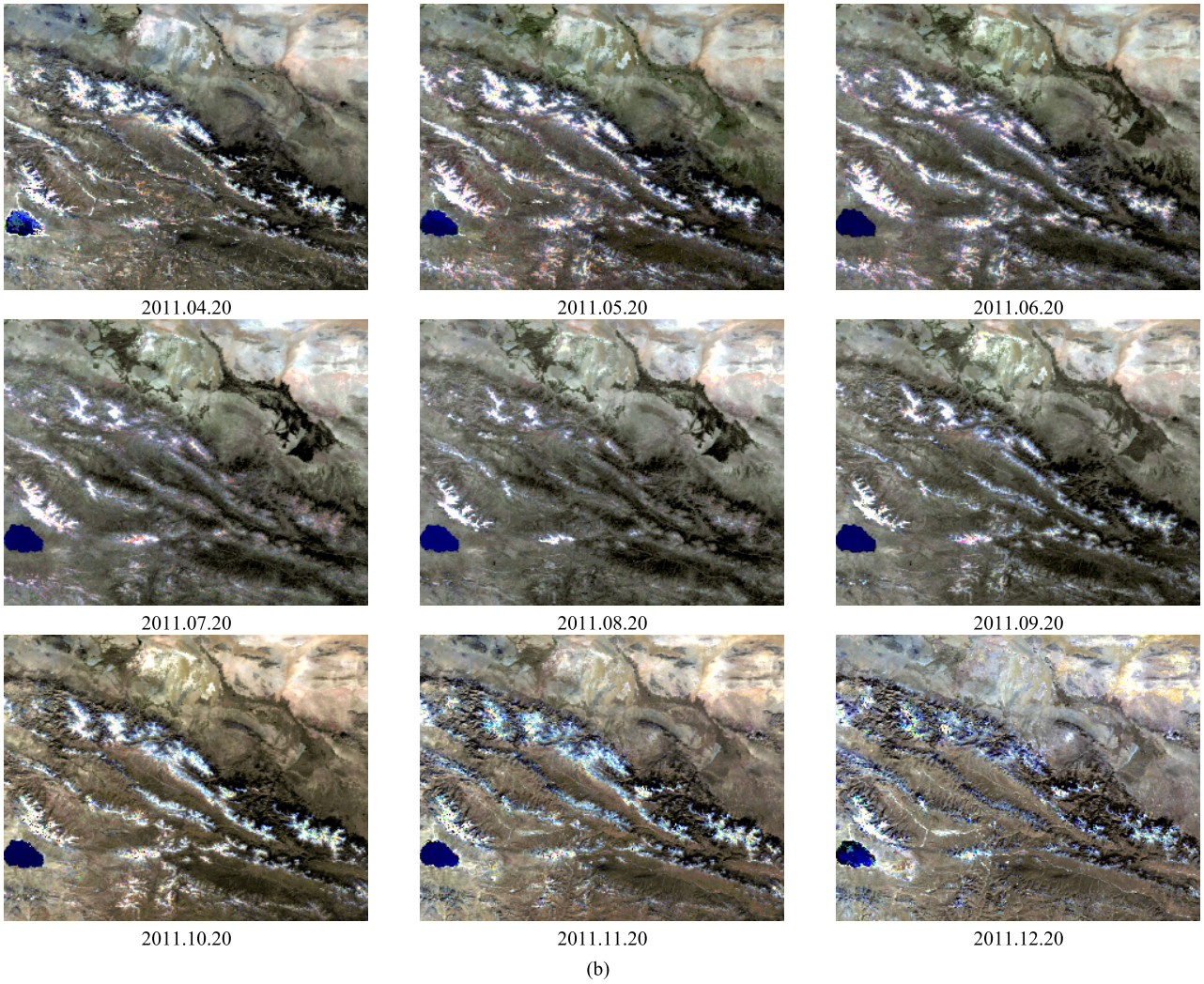

Fig. 10. *(Continued.)* Original and reconstructed MODIS true-color combination time-series images of Zhangye area (the images are selected on the 20th of each month in 2011). (a) Original MODIS true-color combination time series of Zhangye area. (b) Reconstructed MODIS true-color combination time series of Zhangye area.

missing pixels with different percentages for each image on the two test areas. The simulated missing pixels are reconstructed with the real missing pixels by the TSRM method. The quantitative assessment is given in three metrics by comparing reconstructed values with the original values of the simulated missing pixels.

The first metric is the Pearson CC, which measures the degree of similarity between the reconstructed values and the original values. The higher the metric value, the closer will be the two groups of values.

The second metric is the average relative error (ARE) which describes the variations of the value. A smaller value indicates a better prediction. It is described as

$$\mathrm{ARE} = \left(\sum_{j=1}^{M} \left(|g_{\mathrm{re}(j)} - g_{\mathrm{or}(j)}| / g_{\mathrm{or}(j)} \right) \right) \Big/ M \qquad (13)$$

where $g_{\mathrm{re}(j)}$ and $g_{\mathrm{or}(j)}$ are the reconstructed and original values jth missing pixels, respectively. M is the total number of the missing pixels.

The third metric is the root-mean-square error (RMSE) that assesses the deviation of the reconstructed values from the original values. A smaller value indicates a closer similarity between the two groups of values. The RMSE is defined as

$$\mathrm{RMSE} = \sqrt{\sum_{j=1}^{M} (g_{\mathrm{re}(j)} - g_{\mathrm{or}(j)})^2 / (M-1)}. \qquad (14)$$

For the two test areas, 100 and 130 eligible images were selected to be the simulated missing images, respectively. We then calculated three metrics for each band of each image; Figs. 11 and 12 show the comparison curves of three indices for each band of the selected images. For each band of all the images, the results of Step3 almost show a better accuracy than those of Step2 in all indices. The results of Zhangye area are better than those of Wuhan area. Specifically, almost all of the CC values from Step3 on the two test areas are larger than 0.8, and even most of them are larger than 0.9. Only a few images of Wuhan area have a relatively lower CC values less than 0.7. The RMSE is stably less than 0.02, and nearly

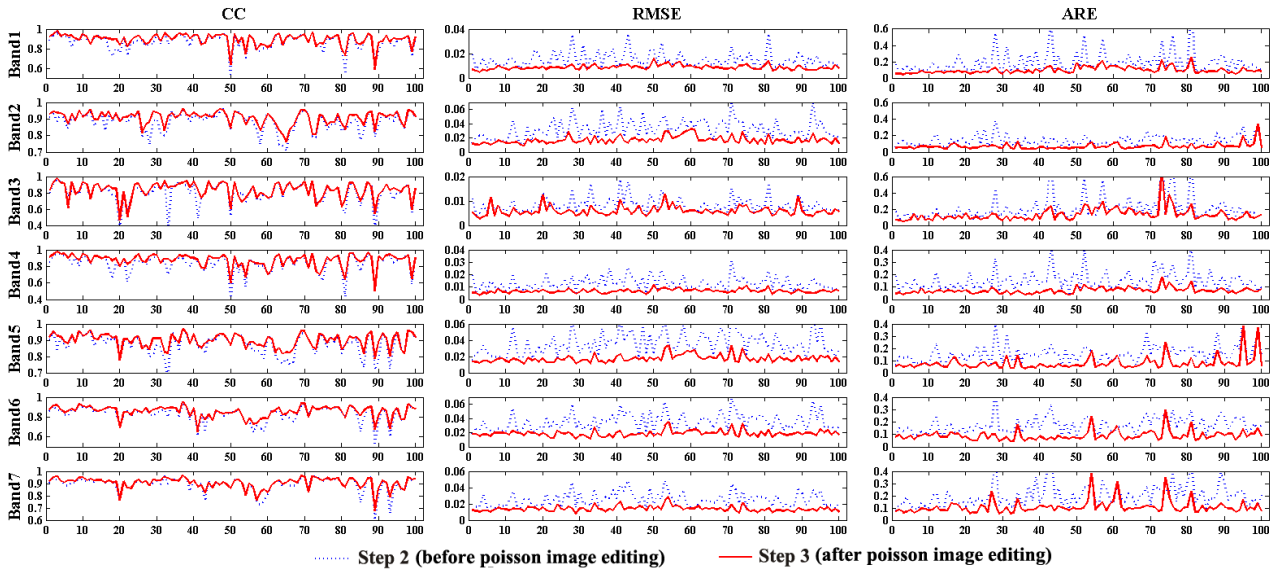

Fig. 11. Comparison curves of Step2 and Step3 for each band of each selected image of Wuhan area. The horizontal axis shows the number of simulated missing images, and the vertical axis denotes the values of three metrics.

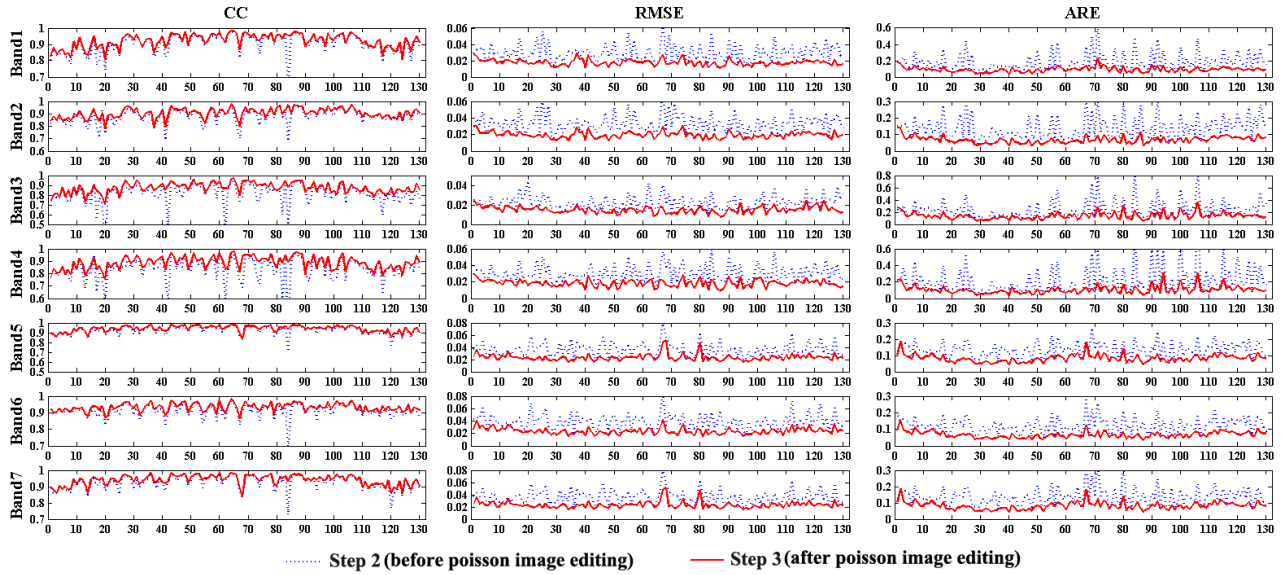

Fig. 12. Comparison curves of Step2 and Step3 for each band of each selected image of Zhangye area. The horizontal axis shows the number of simulated missing images, and the vertical axis denotes the values of three metrics.

all of the results from Step3 have good accuracy. Especially, some of these results are less than 0.01.

Comparing with Step3, Step2 shows lower accuracy but unstable results. Most images reconstructed from Step3 have the good accuracy with the ARE less than 0.1 on the two test areas. Only a few images have high value of ARE larger than 0.2. We guess the partial reason for that is the simulated missing areas of these images might contain many outliers with abnormally high values. Overall, the Poisson image editing is effective in improving the quality of reconstructed results, and the TSRM improves the quality of each band of all the images.

A comprehensive quantitative assessment in three metrics for all the pixels of each band has been further given by comparing the results from Step2 with those from Step3. The quantitative assessment was given, as shown in Table IV. The CC values of Step3 for all the bands on the two test areas are larger than 0.9, and they are larger than the corresponding results of Step2. All the RMSE values of Step3 are smaller than those of Step2, indicating good performance of Poisson image editing. The entire ARE values of Step2 are larger than 0.13, and they are better than those of Step3 that are smaller than 0.13.

In addition, Fig. 13 illustrates the scatter plots of the reconstructed values and the original values. The results of Step2 have large errors, whereas the results of Step3 coincide well with their original values. For different bands, the results of Step2 behave divergently with inconsistent shapes, and the

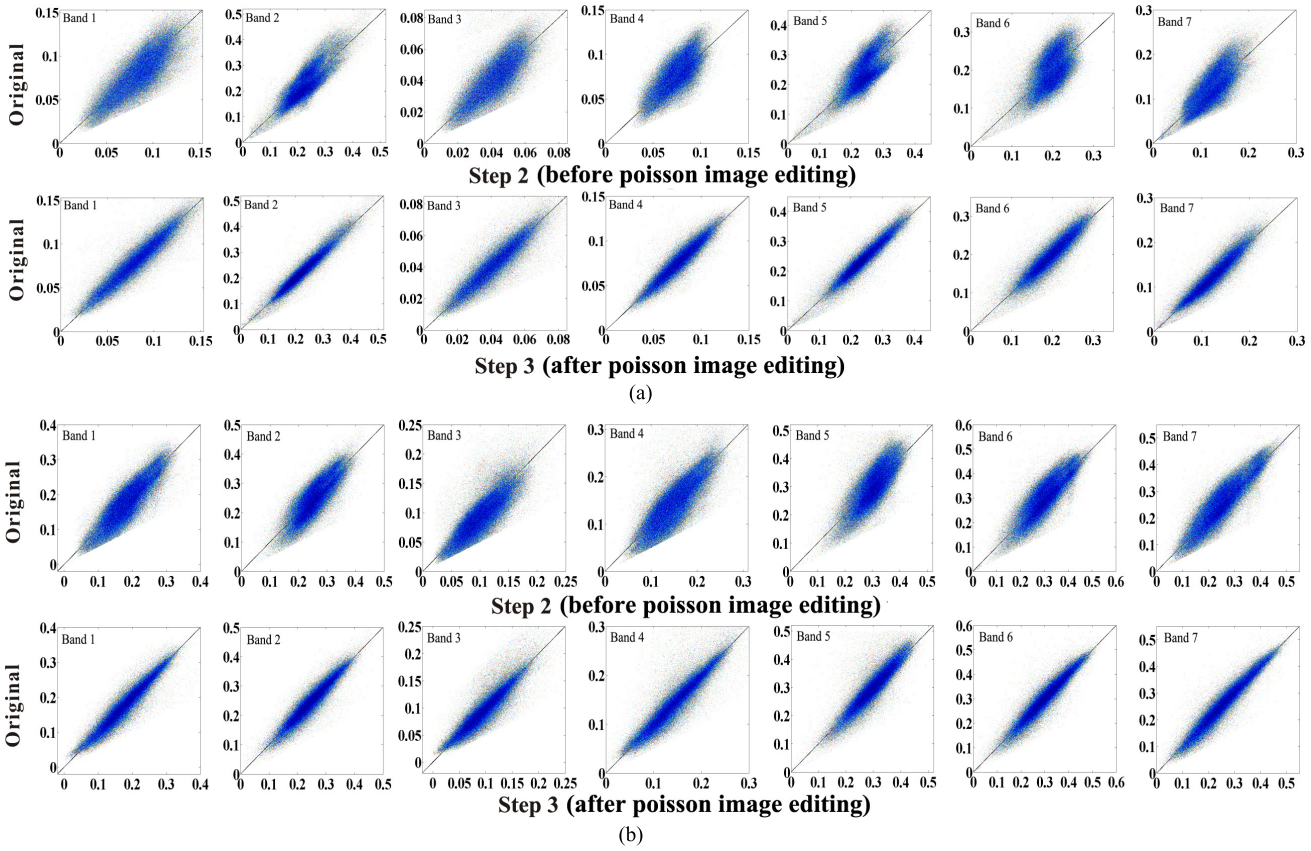

Fig. 13. Scatter plots of the reconstructed results from Step2 and Step3 versus the original values for each band of all the selected simulated images on two test areas. (a) Wuhan area. (b) Zhangye area.

results of Step3 preserve almost the same shape. In summary, the proposed method can effectively reconstruct the missing information with good accuracy.

IV. Conclusion

The original daily surface reflectance data contain large numbers of missing values due to atmospheric contamination or instrument problems. This paper proposes a TSRM to generate daily spatially and temporally complete surface reflectance data. The MODIS MOD09GA and MYD09GA data were selected as the test data, the QA information is used to identify the missing values, and these missing values are filled using the proposed method on seven spectral bands of the MODIS data.

Two test areas were selected to evaluate the performance of the TSRM, and all the results show that the TSRM preserves not only the temporal integrity of the surface reflectance data but also the spatial integrity seamlessly. Moreover, the reconstructed land surface reflectance data maintain the spectral integrity, and different test points show clear seasonal trends in each spectral band image.

The comparison between the results obtained from all three steps (i.e., Step1, Step2, and Step3) shows that the TSRM outperforms the HANTS algorithm in predicting the missing pixels. Specifically, this new method produces spatially and temporally complete data with good accuracy and eliminates the clear seams in the results of the HANTS algorithm.

It should be noted that in Step1, we only selected adjacent two years and three years data as the reference data for Zhangye area and Wuhan area to reduce the probability of land cover change. The explanation is that the land cover types may changes abruptly among different years, and an over long time span might bring about large probability of change in land cover types. If the land cover changes among the two or three years, the first step will result in a great deviation. Considering that, Step2 utilizes the time dependence of the time-series images in the intrayear to adjust the results of Step1 with the true value constraint. Step3 further corrects the results of Step1 and Step2 according to the spatial information. Several parameters should be carefully determined for the HANTS algorithm in Step2. In this paper, we set the parameter "Hilo" as "None." This means that the parameter "NF" is the main factor that affects the final reconstructed result, and that makes the method run faster. The value of NF was manually estimated by our trial experiments, and other parameters, such as the damping factor and DOD, are determined by referring to works by others. The parameter settings are universal because of their little influence on the reconstruction results. However, a little deficiency needs to be discussed. Ideally, the reconstruction of time series at each pixel should have its own optimal parameter of HANTS. Unfortunately, for time-series data reconstruction with a large number of pixels, the automatic optimal selection of parameters is infeasible because dramatically increase the computing time of the algorithm. Considering the efficiency

and generalization capability of the TSRM, we manually adopted the universal empirical values. The fast algorithm for adaptively estimating optimal parameters will be investigated in future research. And all the reconstruction works in this paper use the same parameter settings.

Moreover, the pixels with abnormally high value greatly affect the reconstructed results, and hence, eliminating abnormally high values is very necessary. For example, if some abnormally high-value pixels that exist beyond the boundary of missing areas were wrongly regarded as applicable pixels, the results derived from the Poisson image editing will encounter fuzzy phenomenon around these bad pixels. Finally, this paper is to produce daily gapless and seamless surface reflectance data, and the experiment is implemented on the basic MODIS surface reflectance data (MOD09). These products have been processed to correct most effects, including the BRDF effects. Accordingly, this proposed method allows direct filling of target data through years of reference data without considering the BRDF effects. And the results derived from our method preserve the characteristics of the original data, of which the temporal profiles are with some regular fluctuations.

ACKNOWLEDGMENT

The authors would like to thank the editor and referees for their suggestions that helped improve this manuscript.

REFERENCES

[1] J. Ju, D. P. Roy, Y. Shuai, and C. Schaaf, "Development of an approach for generation of temporally complete daily nadir MODIS reflectance time series," *Remote Sens. Environ.*, vol. 114, no. 1, pp. 1–20, 2010.

[2] J. Zhou, L. Jia, and M. Menenti, "Reconstruction of global MODIS NDVI time series: Performance of Harmonic ANalysis of Time Series (HANTS)," *Remote Sens. Environ.*, vol. 163, pp. 217–228, Jun. 2015.

[3] P. J. Sellers *et al.*, "Modeling the exchanges of energy, water, and carbon between continents and the atmosphere," *Science*, vol. 275, no. 5299, pp. 502–509, 1997.

[4] S. I. Seneviratne *et al.*, "Managing the risks of extreme events and disasters to advance climate change adaptation: Changes in climate extremes and their impacts on the natural physical environment," *J. Clin. Endocr Metab*, vol. 18, no. 6, pp. 586–599, 2012.

[5] C. J. Tucker, "Red and photographic infrared linear combinations for monitoring vegetation," *Remote Sens. Environ.*, vol. 8, no. 2, pp. 127–150, May 1979.

[6] C. O. Justice *et al.*, "An overview of MODIS Land data processing and product status," *Remote Sens. Environ.*, vol. 83, pp. 3–15, Nov. 2002.

[7] R. R. Nemani *et al.*, "Climate-driven increases in global terrestrial net primary production from 1982 to 1999," *Science*, vol. 300, no. 5625, pp. 1560–1563, 2003.

[8] M. Zhao and S. W. Running, "Drought-induced reduction in global terrestrial net primary production from 2000 through 2009," *Science*, vol. 329, no. 5994, pp. 940–943, 2010.

[9] S. Azzali and M. Menenti, "Mapping vegetation-soil-climate complexes in southern Africa using temporal Fourier analysis of NOAA-AVHRR NDVI data," *Int. J. Remote Sens.*, vol. 21, no. 5, pp. 973–996, 2000.

[10] M. Menenti, S. Azzali, W. Verhoef, and R. van Swol, "Mapping agroecological zones and time lag in vegetation growth by means of Fourier analysis of time series of NDVI images," *Adv. Space Res.*, vol. 13, no. 5, pp. 233–237, 1993.

[11] J. R. G. Townshend, "Global data sets for land applications from the Advanced Very High Resolution Radiometer: An introduction," *Int. J. Remote Sens.*, vol. 15, no. 17, pp. 3319–3332, 1994.

[12] B. Ramachandran, C. O. Justice, and M. J. Abrams, *Land Remote Sensing and Global Environmental Change: NASA's Earth Observing System and the Science of ASTER and MODIS*. New York, NY, USA: Springer, 2010.

[13] J. F. Hermance, "Stabilizing high-order, non-classical harmonic analysis of NDVI data for average annual models by damping model roughness," *Int. J. Remote Sens.*, vol. 28, no. 12, pp. 2801–2819, 2007.

[14] H. Shen *et al.*, "Missing information reconstruction of remote sensing data: A technical review," *IEEE Geosci. Remote Sens. Mag.*, vol. 3, no. 3, pp. 61–85, Sep. 2015.

[15] J. Cihlar, D. Manak, and M. D'Iorio, "Evaluation of compositing algorithms for AVHRR data over land," *IEEE Trans. Geosci. Remote Sens.*, vol. 32, no. 2, pp. 427–437, Mar. 1994.

[16] B. N. Holben, "Characteristics of maximum-value composite images from temporal AVHRR data," *Int. J. Remote Sens.*, vol. 7, no. 11, pp. 1417–1434, 1986.

[17] X. Lu, R. Liu, J. Liu, and S. Liang, "Removal of noise by wavelet method to generate high quality temporal data of terrestrial MODIS products," *Photogram. Eng. Remote Sens.*, vol. 73, no. 10, pp. 1129–1139, 2007.

[18] D. P. Roy, "The impact of misregistration upon composited wide field of view satellite data and implications for change detection," *IEEE Trans. Geosci. Remote Sens.*, vol. 38, no. 4, pp. 2017–2032, Jul. 2000.

[19] J. C. Eidenshink and J. L. Faundeen, "The 1 km AVHRR global land data set: First stages in implementation," *Int. J. Remote Sens.*, vol. 15, no. 17, pp. 3443–3462, 1994.

[20] N. Z. El Saleous, E. F. Vermote, C. O. Justice, J. R. G. Townshend, C. J. Tucker, and S. N. Goward, "Improvements in the global biospheric record from the Advanced Very High Resolution Radiometer (AVHRR)," *Int. J. Remote Sens.*, vol. 21, nos. 6–7, pp. 1251–1277, 2000.

[21] C. O. Justice *et al.*, "The Moderate Resolution Imaging Spectroradiometer (MODIS): Land remote sensing for global change research," *IEEE Trans. Geosci. Remote Sens.*, vol. 36, no. 4, pp. 1228–1249, Jul. 1998.

[22] E. G. Moody, M. D. King, S. Platnick, C. B. Schaaf, and F. Gao, "Spatially complete global spectral surface albedos: Value-added datasets derived from Terra MODIS land products," *IEEE Trans. Geosci. Remote Sens.*, vol. 43, no. 1, pp. 144–158, Jan. 2005.

[23] F. Gao, Y. Jin, C. B. Schaaf, and A. H. Strahler, "Bidirectional NDVI and atmospherically resistant BRDF inversion for vegetation canopy," *IEEE Trans. Geosci. Remote Sens.*, vol. 40, no. 6, pp. 1269–1278, Jun. 2002.

[24] D. P. Roy, P. Lewis, C. Schaaf, S. Devadiga, and L. Boschetti, "The global impact of clouds on the production of MODIS bidirectional reflectance model-based composites for terrestrial monitoring," *IEEE Geosci. Remote Sens. Lett.*, vol. 3, no. 4, pp. 452–456, Oct. 2006.

[25] N. Viovy, O. Arino, and A. Belward, "The Best Index Slope Extraction (BISE): A method for reducing noise in NDVI time-series," *Int. J. Remote Sens.*, vol. 13, no. 8, pp. 1585–1590, 1992.

[26] A. Savitzky and M. J. E. Golay, "Smoothing and differentiation of data by simplified least squares procedures," *Anal. Chem.*, vol. 36, no. 8, pp. 1627–1639, 1964.

[27] C. Song, B. Huang, and S. You, "Comparison of three time-series NDVI reconstruction methods based on TIMESAT," in *Proc. IEEE Int. Geosci. Remote Sens. Symp.*, Jul. 2012, pp. 2225–2228.

[28] J. Chen, P. Jönsson, M. Tamura, Z. Gu, B. Matsushita, and L. Eklundh, "A simple method for reconstructing a high-quality NDVI time-series data set based on the Savitzky–Golay filter," *Remote Sens. Environ.*, vol. 91, nos. 3–4, pp. 332–344, 2004.

[29] M. Ma and F. Veroustraete, "Reconstructing pathfinder AVHRR land NDVI time-series data for the Northwest of China," *Adv. Space Res.*, vol. 37, no. 4, pp. 835–840, 2006.

[30] W. Zhu, Y. Pan, H. He, L. Wang, M. Mou, and J. Liu, "A changing-weight filter method for reconstructing a high-quality NDVI time series to preserve the integrity of vegetation phenology," *IEEE Trans. Geosci. Remote Sens.*, vol. 50, no. 4, pp. 1085–1094, Apr. 2012.

[31] Y. Julien and J. A. Sobrino, "Comparison of cloud-reconstruction methods for time series of composite NDVI data," *Remote Sens. Environ.*, vol. 114, no. 3, pp. 618–625, Mar. 2010.

[32] P. Jonsson and L. Eklundh, "Seasonality extraction by function fitting to time-series of satellite sensor data," *IEEE Trans. Geosci. Remote Sens.*, vol. 40, no. 8, pp. 1824–1832, Aug. 2002.

[33] P. S. A. Beck, C. Atzberger, K. A. Høgda, B. Johansen, and A. K. Skidmore, "Improved monitoring of vegetation dynamics at very high latitudes: A new method using MODIS NDVI," *Remote Sens. Environ.*, vol. 100, no. 3, pp. 321–334, 2006.

[34] Y. Julien and J. Sobrino, "Global land surface phenology trends from GIMMS database," *Int. J. Remote Sens.*, vol. 30, no. 13, pp. 3495–3513, 2009.

[35] P. J. Sellers *et al.*, "A global 1° by 1° NDVI data set for climate studies. Part 2: The generation of global fields of terrestrial biophysical parameters from the NDVI," *Int. J. Remote Sens.*, vol. 15, no. 17, pp. 3519–3545, 1994.

[36] W. Verhoef, M. Menenti, and S. Azzali, "Cover A colour composite of NOAA-AVHRR-NDVI based on time series analysis (1981–1992)," *Int. J. Remote Sens.*, vol. 17, no. 2, pp. 231–235, 1996.

[37] G. Yang, H. Shen, L. Zhang, Z. He, and X. Li, "A moving weighted harmonic analysis method for reconstructing high-quality SPOT VEGETATION NDVI time-series data," *IEEE Trans. Geosci. Remote Sens.*, vol. 53, no. 11, pp. 6008–6021, Nov. 2015.

[38] G. J. Roerink, M. Menenti, and W. Verhoef, "Reconstructing cloudfree NDVI composites using Fourier analysis of time series," *Int. J. Remote Sens.*, vol. 21, no. 9, pp. 1911–1917, 2000.

[39] J. Wen, Z. Su, and Y. Ma, "Reconstruction of a cloud-free vegetation index time series for the tibetan plateau," *Mountain Res. Develop.*, vol. 24, no. 4, pp. 348–353, 2009.

[40] R. de Jong, S. de Bruin, A. de Wit, M. E. Schaepman, and D. L. Dent, "Analysis of monotonic greening and browning trends from global NDVI time-series," *Remote Sens. Environ.*, vol. 115, no. 2, pp. 692–702, 2011.

[41] Y. Julien, J. A. Sobrino, and W. Verhoef, "Changes in land surface temperatures and NDVI values over Europe between 1982 and 1999," *Remote Sens. Environ.*, vol. 103, no. 1, pp. 43–55, 2006.

[42] H. Fang *et al.*, "Developing a spatially continuous 1 km surface albedo data set over North America from Terra MODIS products," *J. Geophys. Res. Atmos.*, vol. 112, no. D20206, 2007.

[43] H. Fang, S. Liang, J. R. Townshend, and R. E. Dickinson, "Spatially and temporally continuous LAI data sets based on an integrated filtering method: Examples from North America," *Remote Sens. Environ.*, vol. 112, no. 1, pp. 75–93, Jan. 2008.

[44] A. Verger, F. Baret, M. Weiss, S. Kandasamy, and E. Vermote, "The CACAO method for smoothing, gap filling, and characterizing seasonal anomalies in satellite time series," *IEEE Trans. Geosci. Remote Sens.*, vol. 51, no. 4, pp. 1963–1972, Apr. 2013.

[45] W. Lucht, C. B. Schaaf, and A. H. Strahler, "An algorithm for the retrieval of albedo from space using semiempirical BRDF models," *IEEE Trans. Geosci. Remote Sens.*, vol. 38, no. 2, pp. 977–998, Mar. 2000.

[46] T. Quaife and P. Lewis, "Temporal constraints on linear BRDF model parameters," *IEEE Trans. Geosci. Remote Sens.*, vol. 48, no. 5, pp. 2445–2450, May 2010.

[47] C. Zeng, H. Shen, and L. Zhang, "Recovering missing pixels for Landsat ETM + SLC-off imagery using multi-temporal regression analysis and a regularization method," *Remote Sens. Environ.*, vol. 131, pp. 182–194, 2013.

[48] C. Zeng, H. Shen, M. Zhong, L. Zhang, and P. Wu, "Reconstructing MODIS LST based on multitemporal classification and robust regression," *IEEE Geosci. Remote Sens. Lett.*, vol. 12, no. 3, pp. 512–516, Mar. 2015.

[49] Q. Cheng, H. Shen, L. Zhang, Q. Yuan, and C. Zeng, "Cloud removal for remotely sensed images by similar pixel replacement guided with a spatio-temporal MRF model," *ISPRS J. Photogramm. Remote Sens.*, vol. 92, pp. 54–68, Jun. 2014.

[50] X. Zhang, F. Qin, and Y. Qin, "Study on the thick cloud removal method based on multi-temporal remote sensing images," in *Proc. Int. Conf. Multimedia Technol.*, Oct. 2010, pp. 1–3.

[51] C. H. Lin, P. H. Tsai, K. H. Lai, and J. Y. Chen, "Cloud removal from multitemporal satellite images using information cloning," *IEEE Trans. Geosci. Remote Sens.*, vol. 51, no. 1, pp. 232–241, Jan. 2013.

[52] L. Lorenzi, F. Melgani, and G. Mercier, "Missing-area reconstruction in multispectral images under a compressive sensing perspective," *IEEE Trans. Geosci. Remote Sens.*, vol. 51, no. 7, pp. 3998–4008, Jul. 2013.

[53] X. Li, H. Shen, L. Zhang, H. Zhang, Q. Yuan, and G. Yang, "Recovering quantitative remote sensing products contaminated by thick clouds and shadows using multitemporal dictionary learning," *IEEE Trans. Geosci. Remote Sens.*, vol. 52, no. 11, pp. 7086–7098, Nov. 2014.

[54] E. Vermote and A. Vermeulen, "Atmospheric correction algorithm: Spectral reflectances (MOD09) ATBD version 4.0," Dept. Geogr., Univ. Maryland, College Park, MD, USA, Tech. Rep., 1999.

[55] D. P. Roy, J. S. Borak, S. Devadiga, R. E. Wolfe, M. Zheng, and J. Descloitres, "The MODIS Land product quality assessment approach," *Remote Sens. Environ.*, vol. 83, nos. 1–2, pp. 62–76, 2002.

[56] E. Vermote, S. Kotchenova, and J. Ray, "MODIS surface reflectance user's guide. MODIS Land Surface Reflectance Science Computing Facility," Version 1.3, 2011.

[57] F. L. Gadallah, F. Csillag, and E. J. M. Smith, "Destriping multisensor imagery with moment matching," *Int. J. Remote Sens.*, vol. 21, pp. 2505–2511, Aug. 2000.

[58] H. Shen, P. Wu, Y. Liu, T. Ai, Y. Wang, and X. Liu, "A spatial and temporal reflectance fusion model considering sensor observation differences," *Int. J. Remote Sens.*, vol. 34, no. 12, pp. 4367–4383, 2013.

[59] A. Moody and D. M. Johnson, "Land-surface phenologies from AVHRR using the discrete Fourier transform," *Remote Sens. Environ.*, vol. 75, no. 3, pp. 305–323, 2001.

[60] P. Pérez, M. Gangnet, and A. Blake, "Poisson image editing," *ACM Trans. Graph.*, vol. 22, no. 3, pp. 313–318, Jul. 2003.

[61] E. Vermote, C. O. Justice, and F.-M. Bréon, "Towards a generalized approach for correction of the BRDF effect in MODIS directional reflectances," *IEEE Trans. Geosci. Remote Sens.*, vol. 47, no. 3, pp. 898–908, Mar. 2009.

[62] F.-M. Bréon and E. Vermote, "Correction of MODIS surface reflectance time series for BRDF effects," *Remote Sens. Environ.*, vol. 125, pp. 1–9, Oct. 2012.

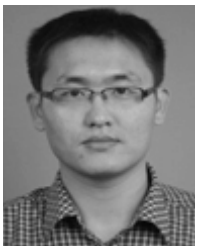

Gang Yang received the M.S. degree in geographical information system from the Hunan University of Science and Technology, Xiangtan, China, in 2012, and the Ph.D. degree from the School of Resource and Environmental Sciences, Wuhan University, Wuhan, China, in 2016.

He is currently an Assistant Professor with Ningbo University, Ningbo, China. His research interests include missing information reconstruction of remote sensing images, cloud removal of remote sensing images, and remote sensing time-series products' temporal reconstruction.

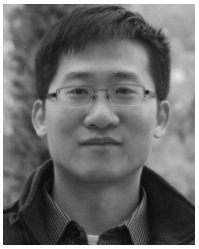

Huanfeng Shen (M'10–SM'13) received the B.S. degree in surveying and mapping engineering and the Ph.D. degree in photogrammetry and remote sensing from Wuhan University, Wuhan, China, in 2002 and 2007, respectively.

In 2007, he joined the School of Resource and Environmental Sciences, Wuhan University, where he is currently a Luojia Distinguished Professor. He has been supported by several talent programs, such as the Youth Talent Support Program of China in 2015, the China National Science Fund for Excellent Young Scholars in 2014, and the New Century Excellent Talents by the Ministry of Education of China in 2011. He has authored over 100 research papers. His research interests include image quality improvement, remote sensing mapping and application, data fusion and assimilation, and regional and global environmental changes.

Dr. Shen is currently a member of the Editorial Board of the *Journal of Applied Remote Sensing*.

Weiwei Sun (M'15) received the B.S. degree in surveying and mapping and the Ph.D. degree in cartography and geographic information engineering from Tongji University, Shanghai, China, in 2007 and 2013, respectively.

From 2011 to 2012, he was a Visiting Scholar with the Department of Applied Mathematics, University of Maryland, College Park, MD, USA, working with the famous Prof. J. Benedetto, studying the dimensionality reduction of hyperspectral image. From 2014 to 2016, he was a Post-Doctoral Researcher with the State Key Laboratory for Information Engineering in Surveying, Mapping and Remote Sensing, Wuhan University, Wuhan, China, studying intelligent processing in hyperspectral imagery. He is currently an Associate Professor with Ningbo University, Ningbo, China. He is also a Visiting Scholar with the Department of Electrical and Computer Engineering, Mississippi State University, Mississippi State, MS, USA. He has authored over 50 journal papers. His research interests include hyperspectral image processing with manifold learning, anomaly detection, and target recognition of remote sensing imagery using compressive sensing.

Jialin Li received the M.S. degree and the Ph.D. degree in physical geography from Nanjing Normal University, Nanjing, China, in 1999 and 2004, respectively.

In 2012, he joined the School of Geosciences, University of South Florida, Tampa, FL, USA, as a Visiting Scholar with the famous Prof. R. Pu, where he studied remote sensing application. He is currently a Professor with Ningbo University, Ningbo, China. His research interests include coastal remote sensing and coastal environmental evolution.

Ninghui Diao received the M.S. degree in physical oceanography from the National Marine Environmental Forecasting Center, Beijing, China, in 2012.

He is currently a Research Assistant with National Satellite Ocean Application Service, Beijing. His research interests include satellite engineering and data preprocessing of remote sensing.

Zongyi He received the B.S. degree and the M.S. degree in cartography from the Wuhan Technical University of Surveying and Mapping, Wuhan, China, in 1982 and 1984, respectively.

He is currently a Full Professor with the School of Resource and Environmental Sciences, Wuhan University, Wuhan. His research interests include digital mapping theory and technology, multiscale spatial data processing, the principles and methods of spatial analysis models, visualization of spatial information, and cartography theory.